Mapping Elastic Properties of Heterogeneous Materials in Liquid with Angstrom-Scale Resolution

Carlos A. Amo[†], Alma. P. Perrino[†], Amir F. Payam, Ricardo Garcia[*]

Materials Science Factory

Instituto de Ciencia de Materiales de Madrid, CSIC

c/ Sor Juana Inés de la Cruz 3, 28049 Madrid, Spain

KEYWORDS

Nanomechanics, bimodal AFM, multifrequency AFM, membrane proteins, metal-organic-frameworks

ABSTRACT. Fast quantitative mapping of mechanical properties with nanoscale spatial resolution represents one of the major goals of force microscopy. This goal becomes more challenging when the characterization needs to be accomplished with subnanometer resolution in a native environment that involves liquid solutions. Here we demonstrate that bimodal atomic force microscopy enables the accurate measurement of the elastic modulus of surfaces in liquid with a spatial resolution of 3 angstroms. The Young's modulus can be determined with a relative error below 5% over a five order of magnitude range (1 MPa-100 GPa). This range includes a large variety of materials from proteins to metal-organic frameworks. Numerical simulations validate the accuracy of the method. About 30 s are needed a Young's modulus map with subnanometer spatial resolution.

The need to provide high resolution maps of material properties is shaping the evolution of atomic force microscopy (AFM).[1-7] Those measurements have been critical to identify the surface structure of thin films block copolymers,[8] to measure the mechanical response of novel materials and devices,[9] or to strengthen the relationship between cell mechanics, physiology and disease.[10] However, none of the above approaches combine subnanometer resolution, quantitative accuracy, fast data acquisition speed, operation in air and liquid and a broad applicability range from soft matter to inorganic crystalline surfaces.

Force microscopy has generated a variety of approaches to measure mechanical properties. Those methods include phase imaging,[11] force volume[12] or multifrequency AFM[6] methods. Those approaches could be classified in two categories, force-distance and parametric methods. Force-distance methods are based on the measurement of the force with respect to the tip-sample distance (force-distance curve) on each point of the surface. Force-distance curves are either obtained by operating the AFM in near-static[12-14] or dynamic modulations.[15-18] A force volume is the map of a surface that contains a force-distance curve on each point of the surface. This approach is widely used to measure with nanoscale spatial resolution the elastic modulus. It has been applied on a large variety of materials such as polymers, layered materials, composites, carbon nanotubes, proteins, cells or tissues.[1, 4,5, 12] However, force volume has several drawbacks. A force-distance curve cannot be obtained at high speed because of the inertial and hydrodynamic effects associated with the cantilever dynamics.[19] In addition, the force constant of the cantilever used in the experiment must be selected according to the elastic response of the material. Consequently, a force volume experiment might not be suitable for mapping the local elasticity of heterogeneous surfaces made of regions with different mechanical properties.

A force volume is commonly generated by operating the AFM in a near-static modulation, although some force volume maps have been recorded with multiharmonics approaches.[15-17] There a force-distance curve is obtained from the time-resolved response. This is performed by processing the higher harmonics components of the cantilever deflection.[5,17] The generation of higher harmonics usually demands the application of forces in the tens or hundreds of nN. Those forces could damage both the tip and the sample. The use of T-shaped cantilevers has enabled to measure the mechanical properties of some synthetic and biological membranes[5,17] at sub-nN forces. Calibration issues and the need of using specifically-designed cantilevers have reduced the applications of this method.

Parametric methods are associated with dynamic AFM.[20-23] In a parametric method the goal is to connect some observables of the microscope with a given mechanical property by using a contact mechanics model. Bimodal AFM is a paradigmatic example of a parametric method.[24] In bimodal AFM two eigenmode frequencies are simultaneously excited and detected.[25] The bimodal observables are very sensitive to changes in the distance.[26,27] This property opened a variety of applications such as the mapping of heterogenenous surfaces,[28,29] imaging of buried nanoparticles[30] or the measurement of the force vector.[31] Bimodal AFM offers a systematic approach to separate magnetic, electrostatic and mechanical interactions from the deflection signal.[32,33] It has been applied to measure the optical properties of surfaces at the nanoscale.[34] The method has also stimulated the design of very sensitive cantilevers.[35]

Bimodal AFM involves the simultaneous excitation and detection of two resonances of the microcantilever, usually the first and the second (Figure 1a). This scheme has given rise to several bimodal AFM configurations depending on the type of feedback controls applied to the excited modes.[24,27,36] Initially an amplitude modulation feedback (AM)

controlled the response of the lowest frequency excited mode while second mode was free to change with the interaction.[37,38] This configuration was sensitive to detect compositional changes but lacked the capability to measure mechanical properties. The exchange of the AM feedback for a frequency modulation feedback (FM) enabled the measurement of the flexibility of a single antibody pentamer.[20] However, this configuration was rather sensitive to changes in the tip geometry or composition. Those changes are easily transformed into operational instabilities while performing measurements in air or liquid. The combination of an AM feedback acting on the first excited mode with a FM feedback acting on the second mode has been proposed as a solution to the aforementioned issues.[24,27,39]

Here we demonstrate that a bimodal force microscopy configuration that combines amplitude and frequency modulation feedbacks (bimodal AM-FM) enables fast, accurate and subnanometer-scale Young's modulus mapping on a wide range of materials in air and liquid. We develop the theoretical approach to transform the observables into Young's modulus and deformation values. We have also developed a numerical simulator to test the validity of the theoretical equations. We demonstrate that bimodal AM-FM provides accurate measurements of the Young's modulus over a 5 order of magnitude range from 1 MPa to 100 GPa. Finally, we provide angstrom-resolved Young's modulus maps of several systems immersed in liquid such as protein membranes, metal-organic frameworks (MOFs) and mica surfaces. Those maps illustrate the accuracy, robustness and the angstrom-scale resolution. Bimodal AM-FM is intrinsically fast because the acquisition of a nanomechanical map does not alter the topographic operation of the AFM.

RESULTS AND DISCUSSION

Theory of bimodal AM-FM force spectroscopy

In bimodal AM-FM the first mode is controlled with an amplitude modulation feedback while the second mode is controlled with a frequency modulation feedback (Figure 1b). The transformation of experimental observables into nanomechanical properties is divided in two major steps. First, the theory that provides the relationship among the experimental observables and the maximum tip-surface force (peak force). The second step involves expressing the peak force in terms of the indentation and the effective Young's modulus by using a contact mechanics model (Figure 1c).

The tip deflection in bimodal AM-FM can be approximated by

$$z(t) = z_0 + \sum_n A_n \cos(\omega_n t - \phi_n) \approx z_0 + A_1 \cos(\omega_1 t - \phi_1) + A_2 \cos(\omega_2 t - \frac{\pi}{2}) \quad (1)$$

where z_0, A_n, $\omega_n = 2\pi f_n$ and ϕ_n are, respectively, the mean deflection, the amplitude, the angular frequency with f_n the oscillation frequency and the phase-shift of the n-th mode. The tip-surface force includes a repulsive force as described by Hertz contact mechanics for a sphere in contact with a flat semi-infinite elastic material,

$$F_{Hertz} = \frac{4}{3} E_{eff} \sqrt{R} \delta^{3/2} \quad (2)$$

where R is the tip-radius, δ is the sample indentation and E_{eff} is the effective Young's modulus of the interface

$$\frac{1}{E_{eff}} = \frac{1 - v_t^2}{E_t} + \frac{1 - v_s^2}{E_s} \quad (3)$$

where E_t and E_s are, respectively, the tip and sample Young moduli; v_t and v_s are, respectively, the tip and sample Poisson coefficients.

The closest tip-sample distance is expressed by

$$d_m = z_c - A_1 - A_2 \tag{4}$$

and whenever $d_m \leq 0$, the indentation is given by

$$\delta = a_0 - d_m \tag{5}$$

where a_0 is molecular diameter, here $a_0 = 0.165$ nm. The parameter z_c is the tip height (mean tip-surface separation).

To relate the observables A_1 and Δf_2 and the material properties E_{eff} and δ by analytical expressions we assume the following hypothesis. (a) The total cantilever displacement can be expressed as a superposition of the excited modes 1 and 2 (eq 1). (b) Average methods such as the virial theorem[40] are independently applied to each of the excited eigenmodes. (c) The feedback control acting on mode 1 does not modify the motion of mode 2 and *vice versa*.

Hölscher and Schwarz[41] showed that in amplitude modulation AFM, whenever A_1 is considerably larger than δ, the closest tip-sample distance d_m can be calculated by

$$d_m = a_0 - \left(\frac{k_1}{Q_1} \frac{A_{N1}}{E_{eff}} \right)^{1/2} \tag{6}$$

$$A_{N1} = \sqrt{\frac{2A_1\left(A_0^2 - A_1^2\right)}{R}} \tag{7}$$

where k_1 and Q_1 are the stiffness and quality factor of the first mode. On the other hand, for a mode controlled by a FM feedback, it has been showed[42] that

$$\Delta f_2 = \sqrt{\frac{R}{8A_1}} \frac{f_{02}}{k_2} E_{eff} \delta \tag{8}$$

By combining eq 4-8, we can determine either the Young's modulus or the indentation,

$$E_{eff} = \frac{k_1}{Q_1} \frac{A_{N1}}{\delta^2} \tag{9}$$

$$\delta = \frac{1}{2} \frac{k_1}{Q_1} \frac{f_{02}}{k_2 \Delta f_2} (A_{01}^2 - A_1^2)^{1/2} \tag{10}$$

We remark that a single observable $\Delta f_2(x,y)$ carries the information about the local changes of the Young's modulus and the indentation. The other parameters that appear in eq 9 and eq 10, k_1, k_2, Q_1, A_{01}, A_1, R and f_{02}, are set at the beginning of the experiment.

A different theoretical approach to obtain analytical expressions has been proposed by Labuda *et al.* [27] They applied the virial equation to determine the change of the force constant of the excited modes under the interaction with the sample. The integrals are determined over the indentation domain by assuming that $A_1 \gg \delta \gg A_2$.

Numerical simulations

To test the theory we have developed a numerical platform that simulates the operation of bimodal AM-FM. Figure 1b shows a simplified scheme of the block diagrams modeled by the simulator. A detailed scheme is provided in the Supporting Information (Figure S1). The cantilever's deflection is processed by three different electronic components in order to obtain the amplitudes and phase shifts of both modes as well as the frequency shift and driving amplitude of the 2nd mode. The amplitudes of the excited modes are kept at fixed values (set-point amplitudes), respectively, A_{sp1} and A_{sp2}. For the first mode this is achieved by adjusting the tip-sample distance while for the 2nd mode, the value A_{sp2} is achieved by varying the driving force of the 2nd mode. In addition, the phase shift of the 2nd mode is processed independently to keep its value fixed at 90º. The simulator also incorporates a tip-sample force model. Then, for a tip-

sample force model the results given by eq 9 and eq 10 are compared with the numerical values produced by the simulator.

Figure 2 compares the results given by the theory and the simulator for three different materials characterized by a Young's modulus of 1 MPa, 1 GPa and 100 GPa. In all cases the sample's Poisson coefficient is 0.3. The probe is characterized by E_{tip}=170 GPa, v_t=0.3 and R= 5 nm. Figure 2a shows the dependence of the Young's modulus with the amplitude ratio for the material with E_s= 1 MPa. The agreement between the sample and the measured value is very good (relative error is below 5 %). The measured value shows a small dependence on the amplitude ratio, however, there is always a range of amplitude ratios that provides the desired accuracy (highlighted in the error insets). For small amplitude ratios, the error increases because the indentation becomes comparable to the value of A_1 (A_{01}=50 nm) (Figure 2b). We remark that eq 9 has been deduced by assuming that A_1 is much larger than δ. Similar results are obtained for the 1 GPa and 100 GPa samples (Figure 2c-f). For the stiffer material (E_s=100 GPa) the agreement covers a wider range of amplitude ratio values (0.3-0.9) (Figure 2e). In this case, the indentation is always below 0.4 nm (Figure 2f), this is, smaller than the values of A_1 (3.6-10.8 nm).

For the three materials, the frequency shift of the 2nd mode increases by decreasing the amplitude ratio. The dependencies of the observables (A_1, A_2, ϕ_1, ϕ_2, Δf_2) on the amplitude ratio are shown in Figure S2 (Supporting Information).

We have also compared the theory and the simulations for other materials with Young's modulus in the 1 MPa-100 GPa range. In all the cases, we have found the existence of a range of amplitude ratios that give a relative error below 5%. The determination of the Young's modulus for stiffer materials (say above 130 GPa) could be problematic

because the Young's modulus of the sample becomes comparable to the one of the tip (170 GPa). Under those conditions, the tip can no longer be considered an underformable sphere. The bimodal AM-FM method could also be applied to very soft materials (say below 1 MPa) provided that cantilevers with small force constants are used.

Angstrom-scale elastic map of a metal-organic-framework surface

To demonstrate the capability of bimodal AFM to provide angstrom-scale (sub-0.5 nm) maps from unprocessed AFM data we have characterized a metal-organic-framework crystal. The measurements also illustrate the broad range of materials amenable for bimodal AFM. The MOF of this study contains metal atoms (cerium) surrounded by oxygen and sulfur atoms.[43] The groups of cerium, oxygen and sulfur atoms are joined by organic linkers. Figure 3a, b shows the atomic structure of the MOF structure[44] (top and side views) with respect to the AFM tip. The lattice parameters a, b and c of the MOF as measured by x-ray crystallography are also given.

A bimodal AM-FM height image (Figure 3c) of a 100x100 nm^2 shows several terraces separated by subnameter step heights (Figure 3d). On the terraces several defects (vacancies) are observed (Figure 3c, e). The defects can be rather small (~4 nm^2). By comparing their size with the atomic structure of the MOF we estimate that they are formed by the removal of about 50 individual atoms.

The bimodal AM-FM height image (Figure 3e) shows a periodic pattern made of an array of parallel lines. One line is made of a discrete sequence of dots while the other appears continuous at the resolution of the image. Between those lines a faint pattern is observed. The line separation is about 1 nm. The image also shows the existence of

several defects (vacancies). The simultaneous presence of a periodic pattern and defects illustrates the true sub-1 nm spatial resolution of the image.

Figure 3f-g shows the topography and Young's modulus maps of the region of the MOF surface marked in Figure 3e. The dashed lines indicate the crystallographic directions marked in Figure 3a. The topography (Figure 3f) shows that between the two major molecular lines there is a line formed by a succession of discrete atomic-like features (~0.2 nm). From the image the measured b, b_1 and b_2 distances are, respectively, 2.1, 1.1 and 0.9 nm. Along the c direction there is a sequence of the discrete structures separated by 0.7 nm. The mean diameter of each discrete structure is about 0.3 nm. Those values are in agreement with the reported structure by X-ray crystallography[43] (Figure 3a). The above Young's modulus maps have been acquired in 26 s.

The elastic modulus map shows four different regions, labelled I, II, III and IV (Figure. 3g). To facilitate the adscription of the observed features with the atomic structure of the MOF layer we have overlaid its atomic structure on the Young's modulus map and performed some cross-section and averaging analysis.

The cross-section (topography) along the lattice direction b shows a periodic pattern with a spatial frequency of 2.1 nm (Figure 4a). The unit of this pattern is made of three near identical peaks and two local minima. The height variation is of 60 pm. The comparison with atomic structure (Figure 3b) indicates that the maxima are associated with the position of Ce atoms while the local minimum happens when the tip is on or near the carbon linkers. The absolute minimum happens when the tip is situated between the carbon linkers. The cross-section obtained from the Young's modulus map indicates that the mechanical response of the Ce atoms depends on the number and type

of atoms that surround them. We measured two peaks, one at about 33 GPa and the other at 30 GPa.

The cross-section along the *c* direction shows a periodic pattern that alternates peaks and valleys with a periodicity of 0.7 nm (Figure 4b). This value is in agreement with the *c* lattice spacing. The same pattern is observed in the topography and Young's modulus cross-sections.

A detailed statistical analysis of the Young's modulus map (Figure 3g) is presented in Figure 4c. The shape of the curve can be decomposed in four individual Gaussian curves centered, respectively, at 25.7 GPa, 27.5 GPa, 29.3 GPa and 32.3 GPa. Those values correspond to the regions labelled I to IV in Figure 3g. The softer regions are likely associated with the regions that lie between the two carbon rings (I). We propose that region II corresponds to the tip directly on top one of the carbon rings (Figure 4d). The rings are laterally separated by 0.35 nm, this is, very close to the spatial resolution shown here (~0.3). Consequently, the map could mix the response of the two rings.

The map shows that the elastic response of the Ce atoms depends on type and number of atoms that surrounding them. Figure 4e and f show that the type and number of the atoms for positions III and IV. Specific atomistic simulations will be needed to explain the details of the observed contrast.

Nanomechanical maps of membrane proteins

Purple membrane (PM) patches are used to calibrate the molecular resolution capabilities of AFM methods in liquid.[45, 46] PM consists of a protein (bacteriorhodopsin, BR) and lipids. The BR forms a hexagonal lattice with a lattice parameter of 6.2 nm. Each lattice point includes three BR (trimer). In the trimer, the proteins form a triangle with a side length of 3 nm. A single BR contains seven

transmembrane α-helices.[47] Schemes of the PM structure and the BR structure are shown in Figure 5a. The loops joining the different α-helices are highlighted in yellow.

Figure 5b shows a bimodal AM-FM image (topography) of several PM patches. The maximum force applied during imaging was of 170 pN. The bimodal AFM image reveals the structure of the patches exposing the extracellular (EC) and the cytoplasmic (CP) surfaces of the membrane. We have also measured the height variations (6 to 8 nm) across the different patches of the PM (Figure S7).

High resolution maps (raw data) of the topography, Young's modulus and deformation of a region of the EC side are shown in Figure 5c-e. The topographic image (Figure 5c) shows the BR trimers and their hexagonal arrangement. The lattice parameter obtained from the image is 6.2 nm. This value matches the value obtained by electron crystallography.[47] The observation of the trimer structure in the unprocessed topography data (Figure 5b-c) indicates a lateral resolution in the sub-2 nm range. This resolution coincides with the best values reported for non-averaged AFM images. [13,48]

The Young's modulus and the deformation maps (raw data) show a regular pattern but the hexagonal structure is not readily evident (Figure 5d-e). To enhance the contrast and the spatial resolution of the nanomechanical maps we have applied cross-correlation and averaging methods[13,48] (see Supporting Information). The processed images are shown in the insets. The BR are arranged on an equilateral triangle of 3 nm side length.

Figure 6a-c shows the topography, the elastic modulus and the deformation maps of a single BR trimer after the application of the averaging method. We have overlaid the structure of the protein in the PM packing as obtained by electron crystallography.[47] The structure of the BR is visualized by using the UCSF Chimera software.[49] The elastic modulus variations along the cross-sections of the extracellular loops B-C, F-G

and D-E are shown, respectively, in Figure 6d, 6e and 6f. Each point of the cross-section represents an average of the values of a region of 1 nm in width. The elastic modulus cross-sections can be correlated with the structure of the protein loops joining the α -helix domains (bottom panels). The elastic response is dominated by α -helix sections with some small contribution associated with the compression of loops. For the B-C loop, the Young's modulus increases from 33 MPa to 41MPa over 1.3 nm. The highest value is obtained in the region where two sections of the loop overlap. From there on E_s decreases to 33 MPa over a distance of 0.7 nm. The F-G loop shows that the Young's modulus grows from 33 MPa to 37 MPa over a distance of 0.4 nm. This region is followed by a plateau at about 37 MPa that extends over 1 nm and then grows to 39 MPa. The D-E loop shows an increase from 33 MPa to 36 MPa. This is followed by a decrease to 33 MPa. We notice that the the Young's modulus in the central region of the α -helix is of 33 MPa. The flexibility of the BR is also plotted in terms of the equivalent stiffness (N/m) of the different loops. We report values between 0.18 and 0.21 Nm^{-1} (See Supporting Information). The measurement of elasticity on the BR changes over 1 nm distances. This observation suggests a subnanometer spatial resolution. This resolution matches the best spatial resolution obtained on the same system with other AFM methods.[13,48]

The elastic modulus and the stiffness of the EC side of the PM have been measured previously. Müller and co-workers[48] deduced the elastic modulus and the stiffness from force-distance curves. They reported values 30 MPa and 0.5 Nm^{-1} across the BR. On the other hand, elastic neutron scattering experiments have reported an average stiffness of 0.33 Nm^{-1}. The bimodal values are consistent with the data reported by both neutron scattering and force-distance curves. We remark that the elastic response of a soft matter system could also depend on the loading rate. For that reason we should not expect to

get exactly the same values from force volume[48] (0.01-2 kHz) and bimodal measurements (5-30 kHz).

The determination of the Young's modulus and/or stiffness depends on the tip's radius R (eq 7). The contact radius can be inferred from the spatial resolution obtained in raw bimodal AFM images (2 nm). From the contact radius and the deformation we deduce a tip radius R of 4 nm.

Discussion

We analyse the factors that explain the bimodal AM-FM capabilities for fast mapping of elastic properties with angstrom-scale resolution in air and/or liquid. The method combines robustness and sensitivity. An AM feedback keeps the amplitude of the 1st mode at a fixed value. This feedback exploits the well-established advantages of tapping mode AFM for stable and high spatial resolution in air or liquid. The FM feedback keeps the phase shift of the 2nd mode 90° with respect to the excitation and at the same time keeps A_2 at a fixed value. Those controls exploit the sensitivity of FM-AFM to detect minor changes in the force or the force gradient. The simultaneous excitation and control of the first two modes enables to establish a system of equations that matches the number of unknowns (material properties) with the number of equations.

High speed AFM has only been achieved by operating the AFM in amplitude modulation.[50] This makes bimodal AM-FM compatible with high speed operation. We have mapped MOF surfaces at a scan rate of 20 Hz. Bimodal AM-FM is also very efficient in terms of data storage. It requires a single data point per pixel to measure the local changes of the Young's modulus and the deformation. A force volume experiment needs about 100 data points per pixel.

The Young's modulus of a material is the ratio between the stress produced by a force applied perpendicular to its surface and the relative deformation (strain) it has produced. At nanoscale, the Young's modulus is defined as the property that results from fitting the AFM data with a contact mechanics model, in particular, the Hertz model. We have demonstrated that this property can be measured with angstrom-scale resolution. However, this definition does not imply the existence of an atomic Young's modulus. The elastic response of an atom depends on its surroundings. This is illustrated in Figure 4a. We have obtained two different values for the position of Ce atoms. The differences in the elastic response are associated with the different type and number of atoms surrounding the Ce.

The accuracy of bimodal AM-FM is demonstrated by the results provided by the numerical simulator. In the simulations we introduce a sample with a well-defined Young's modulus. Then, we test the validity of the theoretical equations to recover the Young's modulus by introducing the parameters of bimodal operation. We have demonstrated that for materials with a Young's modulus in the 1 MPa to 100 GPa range, the relative error is below 5%. The success of the method depends on the suitability of the contact mechanics model to describe the material.

Several years ago, it was reported the identification of individual Si, Pb and Sn surface atoms on a Si surface with an AFM. [51] Their method relies on a precise knowledge of the atomic structure of the tip and on its geometry and chemical stability[52]. Those factors preclude its application outside ultra high vacuum environments. Here we have achieved a lateral resolution of 0.3 nm but with an approach that can be extended to different materials and environments. Bimodal AM-FM does not require a precise knowledge of the tip's structure. It only requires that the tip's apex is more rigid that the sample surface.

CONCLUSION

Bimodal force microscopy has fulfilled a long-standing goal in microscopy, this is, to provide angstrom-resolved maps of the elastic modulus of surfaces in air or liquid. The Bimodal AFM enables the simultaneous acquisition of the topography and the elastic modulus without any limitations on the imaging acquisition rate of the AFM. The method has been applied to measure the elastic modulus of a broad range of materials from biomolecules to inorganic surfaces. The accuracy of the method to determine the elastic in the range from 1 MPa to 100 GPa has been verified by numerical simulations. We have recorded angstrom-resolved maps on a MOF surface in less than 30 s.

The success of the method lies in the asymmetric combination of amplitude and frequency modulation feedbacks. An amplitude modulation feedback applied on the first eigenmode provides a robust and sensitive imaging method for topographic operation in different environments. A frequency modulation feedback acting on the second eigenmode provides the numerical accuracy needed to determine the elastic modulus and the deformation. This bimodal configuration requires just one data point per pixel to determine the elastic modulus and the deformation.

METHODS

Sample preparation

The bimodal AM-FM method was applied to different samples in air and liquid. The samples used for the measurements in air were the polystyrene- polyethylene (PS-LPDE) blend (Bruker, Santa Barbara) and the polystyrene-b-poly(methyl methacrylate) (PS-b-PMMA) block copolymer prepared as described elsewhere[53] (Figure S4).

For the measurements in liquid, three different samples were used: 1) the native PM from *Halobacterium salinarum*. 2) the Cerium Rare-earth Polymeric Framework 8 (Ce-RPF-8), an electric conducting Metal Organic Framework (MOF)[43] and 3) Muscovite mica.

PM patches were deposited on freshly cleaved mica (SPI supplies, USA). Two different buffers were used, one for the sample deposition and the other one for imaging. The deposition buffer contains divalent cations to enhance the PM deposition on the mica surface (10 mM Tris-HCl, 150 mM KCl, 25 mM $MgCl_2$ pH 7.2). 15 µl of deposition buffer and 1 µl of PM solution were mixed. Then, the solution was deposited on a circular piece of mica of 1cm in diameter for 15 minutes. Finally, it was rinsed with imaging buffer (10 mM Tris-HCl, 150 mM KCl pH 7.2). The measurements on the mica surface were performed on freshly cleaved mica in distilled water.

For the MOF measurements, the crystals were immobilized on silicon substrate. A mixture of polydimethylsiloxane (PDMS) (Sylgard 184, Sigma Aldrich) curing agent, PDMS elastomer base and hexane (Scharlau, Scharlab, S.L.), with proportions of 1:10:1000 (by weight) was spin coated on Silicon substrates at 5000 rpm for 60 s. The MOF crystals were then deposited on the PDMS and cured on a hot plate at 80 °C for 40 minutes. After the curing, an ultrasonic treatment of five seconds in distilled water was carried out in order to remove weakly attached crystals. The measurements were performed in a mixture of 80% by volume of distilled water and glycerol (99%, Sigma-Aldrich).

AFM imaging

The bimodal AM-FM developed here was implemented into a commercial AFM (Cypher, Asylum Research). The acquisition time for the high resolution images on the PM (512x512 pixel, 6 Hz) (Figure 6), the mica (256x256 pixel, 7 Hz) (Figure S6) and the MOF (512x512 pixel, 20 Hz) (Figure 3) have been 90 s, 36 s and 26s, respectively.

The data reported here has been taken with three cantilevers. Purple membrane (PM) patches (Figure 5 and Figure S7) were imaged with a AC-40TS cantilever (Olympus, Japan) characterized by f_{01}=26.4 kHz, f_{02}=225.5 kHz, Q_1=2, k_1= 79.83 pN/nm and k_2= 4.45 N/m in liquid. The free amplitudes used in Figure 3 were A_{01}= 3.5 nm and A_{02}=0.35 nm and the image was taken at A_{sp}=A_1/ A_{01}=0.9. The free amplitudes used to take Figure S5 were A_{01}= 4.4 nm, A_{02}=0.35 nm and A_{sp}=A_1/ A_{01}=0.8. The tip radius, R, used to calculate Figure 5c and d was 4 nm.

The maps of the freshly cleaved mica (Figure S6) were obtained in distilled water with a PPP-NCH cantilever (Nanosensors, Switzerland) characterized by f_{01}= 125 kHz, f_{02}= 870 kHz, Q_1= 8, k_1= 30 N/m and k_2= 1313 N/m in liquid. The image was taken at A_{sp}= 0.6 with free amplitudes of A_{01}=1.8 nm and A_{02}= 0.14 nm. The value of R applied to determine Figure S6b was 2 nm. The PPP-NCH cantilever was also used to measure the polymer blend (Figure S4). The experimental values for the cantilever were f_{01}= 320 kHz, f_{02}= 1981 kHz, Q_1= 420, k_1= 39 N/m and k_2= 1860 N/m measured in air. The tip radius, R, used to calculate Figure S4 b and c was 18 nm.

Finally, an Arrow-UHF cantilever (Nanoworld AG, Switzerland) was used for the metal – organic framework (MOF) crystals (Fig 3). The experimental values for the cantilever were f_{01}= 293 kHz, f_{02}= 1091 kHz, Q_1=1.5, k_1= 5 N/m, k_2= 60 N/m measured in liquid. The amplitudes used to obtain Figure 3 were A_{01}= 1.05 nm and A_{02}= 0.1 nm and at A_{sp}= 0.7. The tip parameter, R, applied to calculate Figure 3d was 0.5 nm.
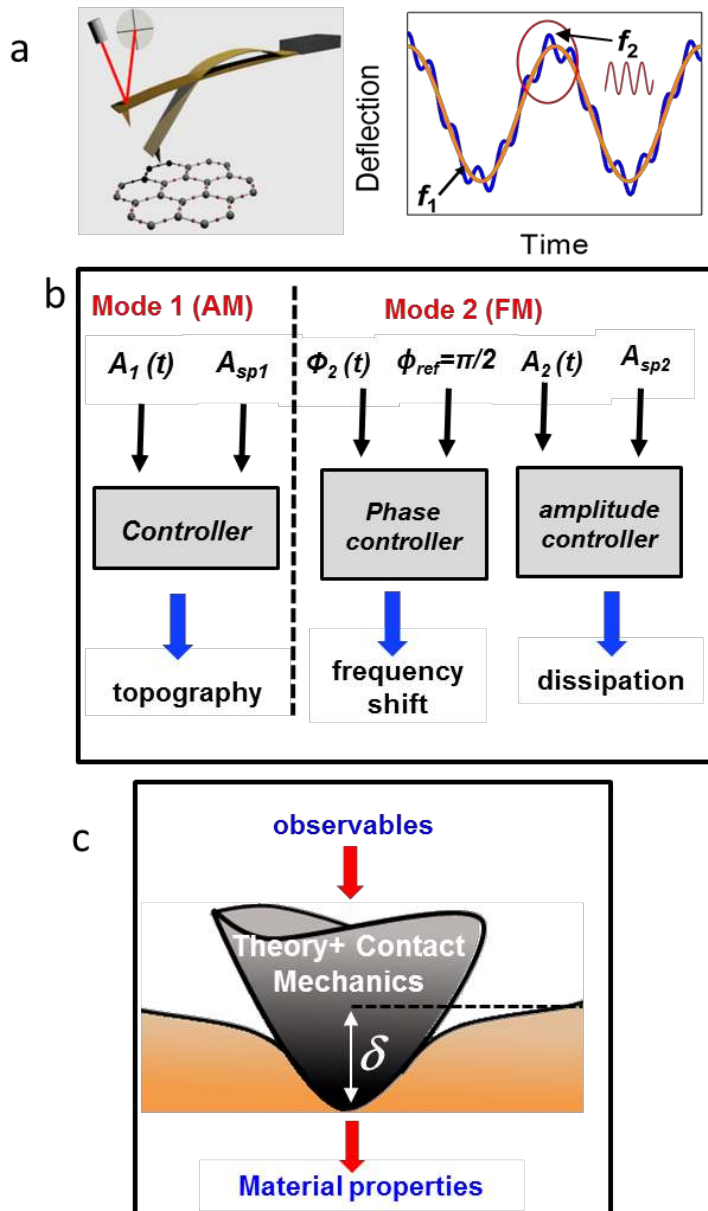
FIGURES

Figure 1. Imaging and force spectroscopy in bimodal AM-FM. (a) Scheme of the cantilever deflection during bimodal operation. The deflection signal carries two components. The low frequency component is tuned at the 1st resonant frequency of the cantilever and the high frequency component is tuned at the 2nd eigenmode frequency. (b) Simplified scheme of the feedback loops in bimodal AM-FM. The topography feedback operates on the amplitude of the 1st mode like in regular amplitude modulation (tapping mode) AFM imaging. The phase shift of the 2nd mode is kept at 90° with

respect to the driving force while the A_2 is kept at a fixed value (A_{sp2}). The last step is achieved by varying the driving force that excites the 2nd mode. This process is called dissipation. (c) Simplified scheme of the transformation of bimodal data into nanomechanical properties. The theory includes the description of the microcantilever dynamics and a contact mechanics model.
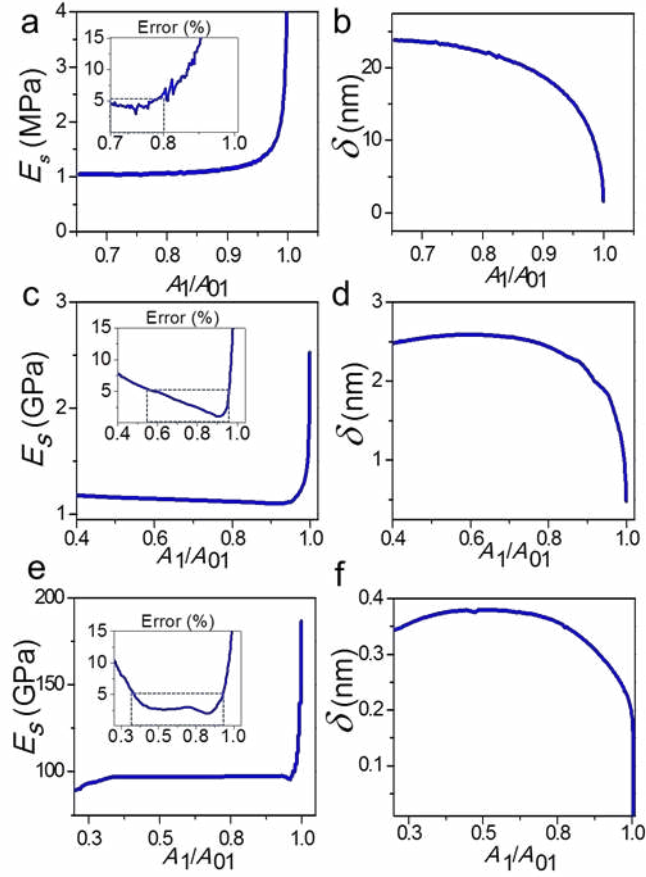
Figure 2. Simulation of bimodal nanomechanical spectroscopy measurements. (a) Determination of the Young's modulus as a function of the amplitude ratio for a sample of E_s= 1 MPa. (b) Indentation for the same material. Parameters in *a* and *b*: A_{01}= 50 nm, A_{02}=0.5 nm, k_1=0.01 N/m, k_2=2 N/m, Q_1=2.3, f_{01}=31.7 kHz, f_{02}=263.5 kHz. **c**, Measured Young's modulus as a function of the amplitude ratio for a sample of E_s= 1 GPa. (d) Indentation for the same material. Parameters in *c* and *d*: A_{01}= 10 nm, A_{02}=1 nm, k_1=5 N/m, k_2=40 N/m, Q_1=2.3, f_{01}=100 kHz, f_{02}=628 kHz. (e) Measured Young's modulus as a function of the amplitude ratio for a sample of E_s= 100 GPa. (f) Indentation for the same material. Parameters in *e* and *f*: A_{01}= 5 nm, A_{02}=0.1 nm, k_1=30 N/m, k_2=1313 N/m, Q_1=2.3, f_{01}=129 kHz, f_{02}=876 kHz. In all the simulations: E_{tip}=170 GPa, v_t=v_s=0.3 and R= 5 nm. The insets show the relative error as a function of the amplitude ratio.
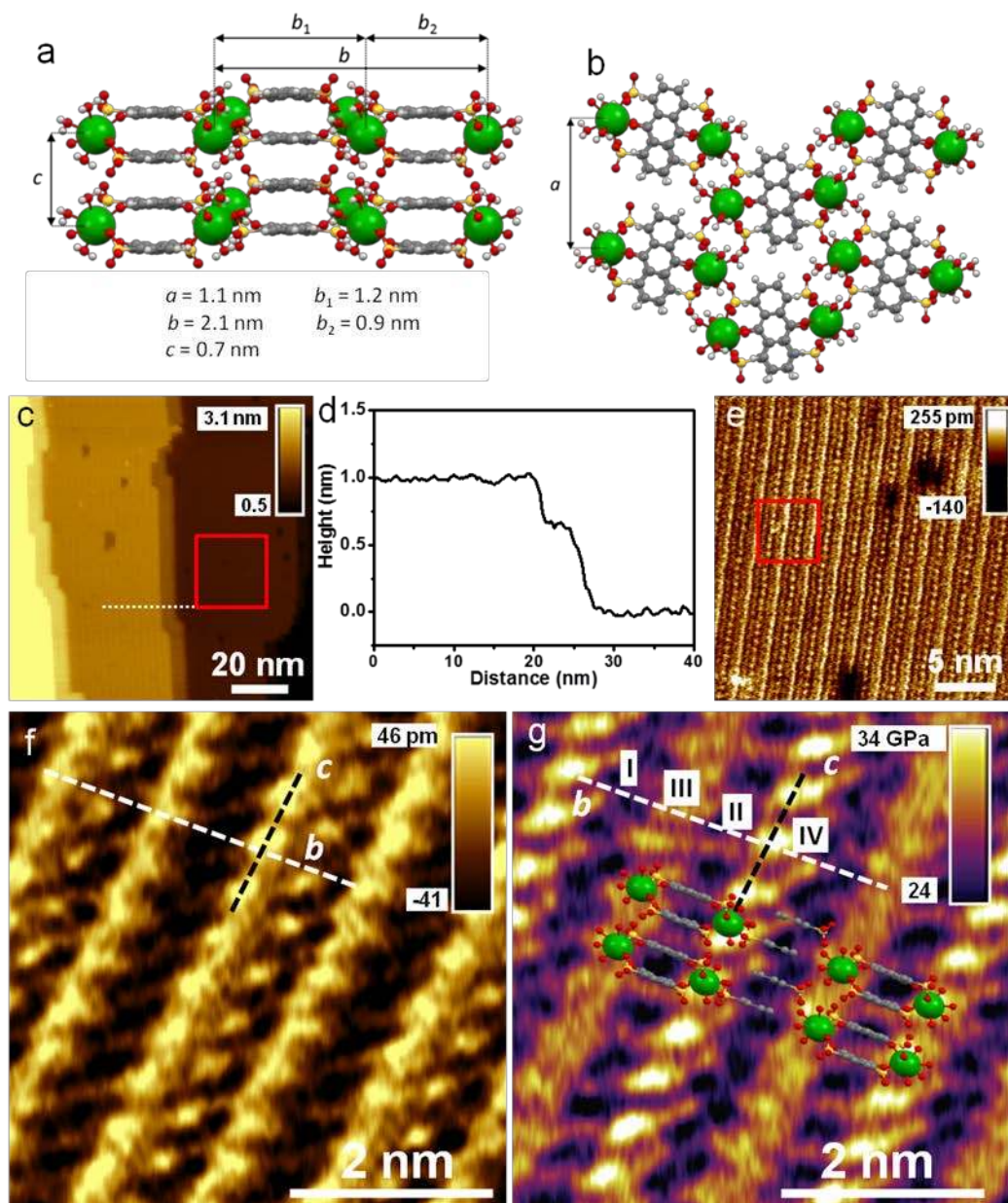
Figure 3. Elastic modulus map of a metal-organic-framework. (a) Top view structure of the metallic-organic-framework. Atom colors: Ce, green; S, yellow; O, red; C, gray; H, white. (b) Side view structure of the MOF. The atoms are scaled to their respective atomic radius. (c) Bimodal AFM image (topography) of a section of the MOF surface. (d) Height cross-section along the line marked in *c*. (e) Subnameter-resolved image of the region of the MOF marked in *c*. (f) Angstrom-resolved bimodal (topographic) image

of the region of the MOF marked in *e*. (g) Elastic modulus map of the region shown in *f*.

The MOF structure on the basal plane has been overlaid. Bimodal AM-FM parameters:

A_{01}=1.05 nm, A_{02}=0.1 nm; k_1=5 N/m, k_2=60 N/m, Q_1=2; f_{01}=293 kHz, f_{02}=1091kHz,
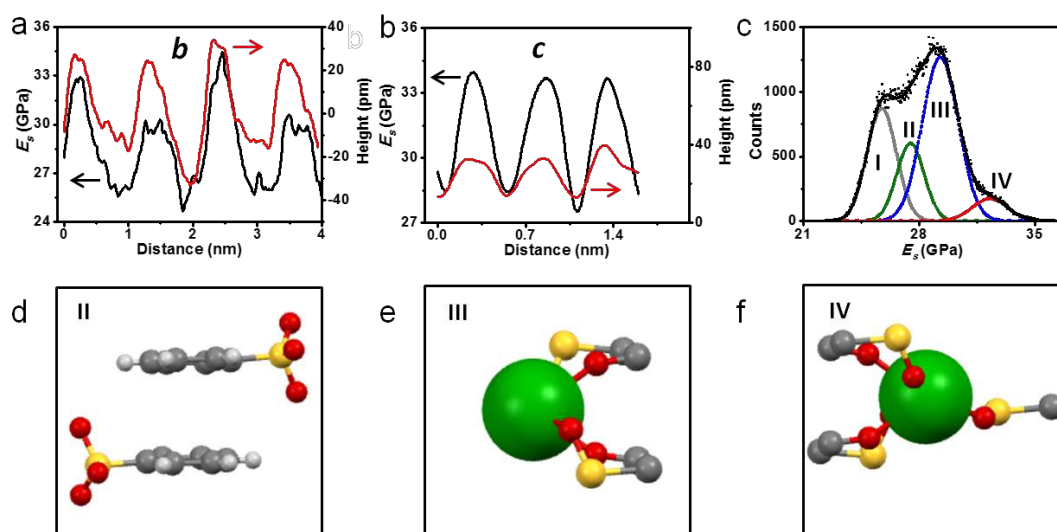
E_{tip}=170 GPa, v_t=v_s=0.3 and R= 0.5 nm.

Figure 4. Cross-sections and statistical Young's modulus curves. (a) Topography and Young's modulus cross-sections along the dashed lines parallel to the *b* lattice vector. (b) Topography and Young's modulus cross-sections along the dashed lines parallel to the *c* lattice vector. (c) Statistic elastic modulus values obtained over the region shown in Figure 3g. The curve can be decomposed in four individual Gaussian curves, centered respectively, at 25.7, 27.5, 29.3 and 32.3 GPa. (d) Atomic structure associated with a Young's modulus of 27.5 GPa. (e) Proposed atomic structure for the locations that give a Young's modulus of 29.3 GPa. (f) Atomic structure associated with the positions that give a Young's modulus of 32.3 GPa. In panels *e* and *f* we have omitted all H atoms for clarity. Atom colors: Ce, green; S, yellow; O, red; C, gray; H, white.
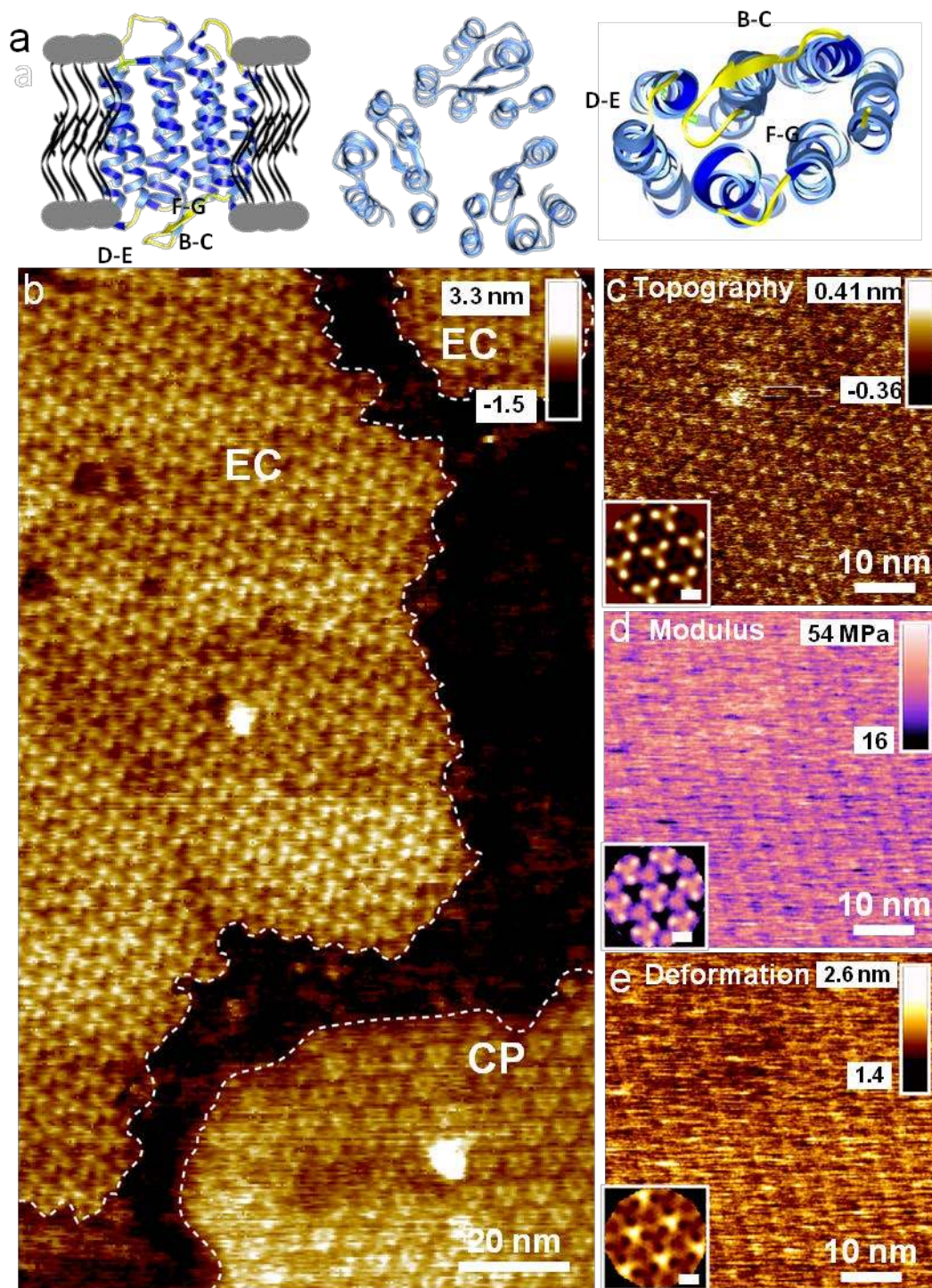
Figure 5. Bimodal AFM maps of a purple membrane in buffer. (a) Topography of several PM patches showing the extracellular and the cytoplasmic sides of the membrane. (b) High resolution image of an EC region of the membrane. The hexagonal arrangement of the BR trimmers is resolved. (c) Young's modulus map of the region shown in b. The image (raw data) shows the existence of parallel stripes with a spacing of 6.2 nm. (d) Indentation map of the region shown in b. A_{01}=4.4 nm, A_{02}=0.35 nm,

k_1=0.08 N/m, k_2=4.45 N/m, Q_1=2; f_{01}=26.4 kHz, f_{02}=225 kHz; E_{tip}=170 GPa, v_t=v_s=0.3 and R= 4 nm. The insets in c, d and e show the three-fold symmetrized averages of each channel. Scale bars, 2 nm. More data on the conditions to obtain the above maps are provided in the Supporting Information.
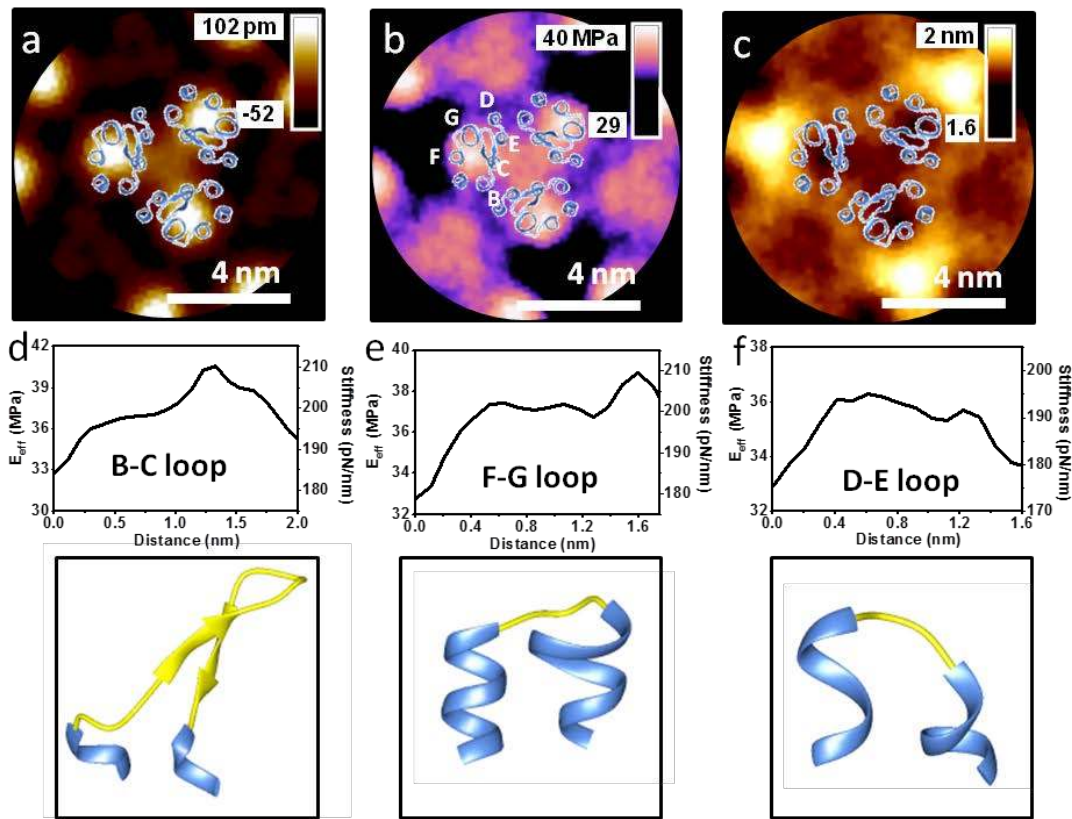
Figure 6. Cross-correlation maps of a BR trimer. (a) Three-fold symmetrized averages of the topographic image. (b) Three-fold symmetrized averages of the modulus map. (c) Three-fold symmetrized averages of the deformation map. The structure of the BR is overlaid. (d) Young's modulus cross-section along the B-C loop. E. Young's modulus cross-section along the F-G loop. F. Young's modulus cross-section along the D-E loop. The three extracellular loops B-C, F-G and D-E are plotted in yellow.

For Table of Contents Only
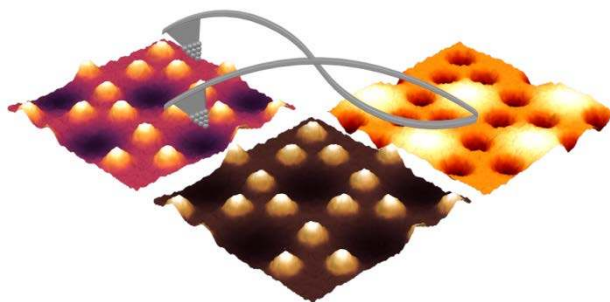
ASSOCIATED CONTENT

Supporting Information

Additional figures and information about the numerical simulator, probe calibration method, sample preparation, AFM imaging and data processing are provided *via* Supporting Information. This material is available free of charge *via* the Internet at http://pubs.acs.org.

AUTHOR INFORMATION

Corresponding Author

*Prof. Ricardo Garcia, r.garcia@csic.es

Present address

(A.F.P.) Department of Physics, Durham University, Durham DH1 3LE, UK

Author contributions

The manuscript was written through contributions of all authors. All authors have given approval to the final version of the manuscript. ‡ Carlos A. Amo and Alma P. Perrino contributed equally to this manuscript.

REFERENCES

1 Dufrêne, Y. F.; Ando, T.; Garcia, R.; Alsteens, D.; Martinez-Martin, D.; Engel, A.; Gerber, G.; Müller, D. J. Imaging Modes of Atomic Force Microscopy for Application in Molecular and Cell Biology. *Nat. Nanotechnol*. **2017**, *12*, 295-307.

2 Santos, S.; Lai, C. Y.; Olukan, T.; Chiesa, M. Multifrequency AFM: from Origins to Convergence. *Nanoscale* **2017**, *9***,** 5038.

3 Kalinin, S.V.; Strelcov, E.; Belianinov, A.; Somnath, S.; Vasudevan, R. K.; Lingerfelt, E. J.; Archibald, R. K.; Chen, C.; Proksch, R.; Laanait, N.; Jesse, S. Big, Deep, and Smart Data in Scanning Probe Microscopy. *ACS Nano* **2016**, *10***,** 9068-9086.

4 Chyasnavichyus, M.; Young, S. L.; Tsukruk, V. V. Recent Advances in Micromechanical Characterization of Polymer, Biomaterial, and Cell Surfaces with Atomic Force Microscopy. *Jpn. J. Appl. Phys.* **2015**, *54*, 08LA02-1 – 13.

5 Zhang, S.; Aslan, H.; Besenbacher, F.; Dong, M. Quantitative Biomolecular Imaging by Dynamic Nanomechanical Mapping. *Chem. Soc. Rev.* **2014**, *43*, 7412 – 7429.

6 Garcia, R.; Herruzo, E. T. The Emergence of Multifrequency Force Microscopy. *Nat.Nanotechnol*. **2012**, *7*, 217-226.

7 Cohen, S. R.; Kalfon – Cohen, E. Dynamic Nanoindentation by Instrumented Nanoindentation and Force Microscopy: a Comparative Review. *Beilstein J. Nanotechnol.* **2013**, *4*, 815 – 833.

8 Knoll, A.; Horvat, A.; Lyakhova, K. S.; Krausch, G.; Sevink, G. J. A.; Zvelindovsky, A. V.; Magerle, R. Phase Behavior In Thin Films Of Cylinder-Forming Block Copolymers. *Phys. Rev. Lett.* **2002**, *89*, 035501.

9 Lopez-Polin, G.; Gómez-Navarro, C.; Parente, V.; Guinea, F.; Katsnelson, M. I.; Pérez-Murano, F.; Gómez-Herrero, J. Increasing the Elastic Modulus of Graphene by Controlled Defect Creation. *Nat. Phys.* **2015**, *11*, 26-31.

10 Lekka, M.; Pogoda, K.; Gostek, J.; Kylmenko, O.; Prauzner-Bechcicki, S.; Wiltowska-Zuber, J.; Jaczewska, J.; Lekki, J.; Stachura, Z. Cancer Cell Recognition - Mechanical Phenotype. *Micron* **2012**, *43*, 1259-1266.

11. Garcia, R.; Magerle, R.; Pérez, R. Nanoscale Compositional Mapping with Gentle Forces. *Nat. Mater.* **2007**, *6*, 405-411.

12. Dufrêne, Y. F.; Martínez – Martín, D.; Medalsy, I.; Alsteens, D.; Müller, D. J. Multiparametric Imaging of Biological Systems by Force – Distance Curve – Based AFM. *Nat. Methods* **2013**, *10*, 847 – 854.

13 Rico, F.; Su, C.; Scheuring, S. Mechanical Mapping of Single Membrane Proteins at Submolecular Resolution. *Nano Lett.* **2011**, *11*, 3983 – 3986.

14 Dokukin, M. E.; Sokolov, I. Quantitative Mapping of the Elastic Modulus of Soft Materials with HarmoniX and PeakForce QNM AFM Modes. *Langmuir* **2012**, *28*, 16060–16071.

15 Stark, M.; Stark, R.W.; Heckl W.M.; Guckenberger R. Inverting Dynamic Force Microscopy: from Signals to Time-Resolved Interaction Forces. *Proc. Natl. Acad. Sci. U.S.A.* **2002**, *99*, 8473.

16 Sahin, O.; Magonov, S.; Su, C.; Quate, C. F.; Solgaard, O. An Atomic Force Microscope Tip Designed to Measure Time – Varying Nanomechanical Forces. *Nat. Nanotechnol.* **2007**, *2*, 507–514.

17 Shamitko-Klingensmith, N.; Molchanoff, K. M.; Burke, K. A.; Magnone, G. J.; Legleiter, J. Mapping the Mechanical Properties of Cholesterol-Containing Supported Lipid Bilayers with Nanoscale Spatial Resolution. *Langmuir* **2012**, *28*, 134111-13422.

18 Forchheimer, D.; Forchheimer, R.; Haviland, D. B. Improving Image Contrast and Material Discrimination with Nonlinear Response in Bimodal Atomic Force Microscopy. *Nat. Commun.* **2015**, *6*, 6270.

19 Amo, C.A.; Garcia, R. Fundamental High-Speed Limits in Single-Molecule, Single-Cell and Nanoscale Force Spectroscopies. *ACS Nano* **2016**, *10*, 7117.

20 Martinez-Martin, D.; Herruzo, E.T.; Dietz, C.; Gomez-Herrero, J.; Garcia, R. Noninvasive Protein Structural Flexibility Mapping by Bimodal Dynamic Force Microscopy. *Phys. Rev. Lett.* **2011**, *106*, 198101.

21 Cartagena-Rivera, A. X.; Wang, W. H.; Geahlen, R. L.; Raman, A. Fast, Multi-Frequency, and Quantitative Nanomechanical Mapping of Live Cells Using the Atomic Force Microscope. *Sci. Rep.* **2015**, *5*, 11692.

22 Killgore, J. P.; Yablon, D. G.; Tsou, A. H.; Gannepalli, A.; Yuya, P. A.; Turner, J. A.; Proksch, R.; Hurley, D. C. Viscoelastic Property Mapping with Contact Resonance Force Microscopy. *Langmuir* **2011**, *27*, 13983-13987.

23 Saraswat, G.; Agarwal, P.; Haugstad, G.; Salapaka, M. V. Real-Time Probe Based Quantitative Determination of Material Properties at The Nanoscale. *Nanotechnology* **2013**, *24*, 265706.

24 Garcia, R.; Proksch, R. Nanomechanical Mapping of Soft Matter by Bimodal Force Microscopy. *Eur. Polym. J.* **2013**, *49*, 1897 – 1906.

25 Rodriguez, T. R; Garcia, R. Compositional Mapping of Surfaces in Atomic Force Microscopy by Excitation of The Second Normal Mode of The Microcantilever. *Appl.Phys. Lett*. **2004**, *84*, 449-451.

26 Kawai, S.; Glatzel, T.; Koch, S.; Such, B.; Baratoff, A.; Meyer, E. Systematic Achievement of Improved Atomic-Scale Contrast *via* Bimodal Dynamic Force Microscopy. *Phys. Rev. Lett.* **2009**, *103*, 220801.

27 Labuda, A.; Kocun, M.; Meinhold, W.; Walters, D.; Proksch, R. Generalized Hertz Model for Bimodal Nanomechanical Mapping. *Beilstein J. Nanotechnol.* **2016**, *7*, 970-982.

28 Nguyen, H. K.; Ito, M.; Nakajima, K. Elastic and Viscoelastic Characterization of Inhomogeneous Polymers by Bimodal Atomic Force Microscopy. *Jpn. J. Appl. Phys.* **2016**, *55*, 08NB06.

29 Lai, C. Y.; Santos, S.; Chiesa, M. Systematic Multidimensional Quantification of Nanoscale Systems from Bimodal Atomic Force Microscopy Data. *ACS Nano* **2016**, *10*, 6265-6272.

30 Ebeling, D.; Eslami, B.; Solares, S. D. Visualizing the Subsurface of Soft Matter: Simultaneous Topographical Imaging, Depth Modulation, and Compositional Mapping with Triple Frequency Atomic Force Microscopy. *ACS Nano* **2013**, *7*, 10387-10396.

31 Naitoh, Y.; Turanský, R.; Brndiar, J.; Li, Y. J.; Štich, I.; Sugawara, Y. Subatomic-Scale Force Vector Mapping above a Ge(001) Dimer Using Bimodal Atomic Force Microscopy. *Nat. Phys.* **2017**, *13,* 663–667.

32 Stark, R. W.; Naujoks, N.; Stemmer, A. Multifrequency Electrostatic Force Microscopy in the Repulsive Regime. *Nanotechnology* **2007**, *18*, 065502.

33 Schwenk, J.; Zhao, X.; Bacani, M. A.; Romer, S.; Hug, H. J. Bimodal Magnetic Force Microscopy with Capacitive Tip-Sample Distance Control. *Appl. Phys. Lett.* **2015**, *107*, 132407.

34. Ambrosio, A.; Devlin, R. C.; Capasso, F.; Wilson, W. L. Observation of Nanoscale Refractive Index Contrast *via* Photoinduced Force Microscopy. *ACS Photonics* **2017**, *4*, 846-851.

35 Penedo, M.; Hormeño, S.; Prieto, P.; Alvaro, R.; Anguita, J.; Briones, F.; Luna, M. Selective Enhancement of Individual Cantilever High Resonance Modes. *Nanotechnology* **2015**, *26*, 485706.

36 Chawla, G.; Solares, S.D. Mapping of Conservative and Dissipative Interactions in Bimodal Atomic Force Microscopy Using Open-Loop And Phase-Locked-Loop Control of the Higher Eigenmode. *Appl. Phys. Lett.* **2011**, *99*, 074103.

37 Martinez, N. F.; Patil, S.; Lozano, J. R.; Garcia, R. Enhanced Compositional Sensitivity in Atomic Force Microscopy by the Excitation of the First Two Flexural Modes. *App. Phys. Lett.* **2006**, *89*, 153115.

38 Proksch, R. Multifrequency, Repulsive – Mode Amplitude – Modulated Atomic Force Microscopy. *Appl. Phys. Lett.* **2006**, *89*, 113121.

39 Kocun, M.; Labuda, A.; Meinhold, W.; Revenko, I.; Proksch, R. High-Speed, Wide Modulus Range Nanomechanical Mapping with Bimodal Tapping Mode. *arXiv.org* **2017**, arXiv:1702.06842.

40 Lozano, J. R.; Garcia, R. Theory of Phase Spectroscopy in Bimodal Atomic Force Microscopy. *Phys. Rev. B* **2009**, *79*, 014110.

41 Hölscher, H.; Schwarz, U. D. Theory of Amplitude Modulation Atomic Force Microscopy with and without Q-Control. *Int. J. Non-Linear Mech.* **2007**, *42*, 608-625.

42 Herruzo, E. T.; Perrino, A. P.; Garcia, R. Fast Nanomechanical Spectroscopy of Soft Matter. *Nat. Commun.* **2014**, *5*, 3126-3204.

43. Gándara, F.; Snejko, N., de Andrés, A.; Fernandez, J. R., Gómez- Sal, J. C., Gutierrez – Puebla, E., Monge, A. Stable Organic Radical Stacked by *In Situ* Coordination to Rare Earth Cations in MOF Materials. *RSC Adv.* **2012**, *2*, 949-955.

44. Macrae, C. F.; Bruno, I. J.; Chisholm, J. A.; Edgington, P. R.; McCabe, P.; Pidcock, E. Rodriguez-Monge, L.; Taylor, R.; van de Streek, J.; Wood, P. A. *Mercury CSD 2.0 – New Features for the Visualization and Investigation of Crystal Structures. J. Appl. Cryst.* **2008**, *41*, 466-470.

45 Fechner, P.; Boudier, T.; Mangenot, S.; Jaroslawski, S.; Sturgis, J. N.; Scheuring, S. Structural Information, Resolution, and Noise In High-Resolution Atomic Force Microscopy Topographs. *Biophys. J.* **2009**, *96*, 3822-3831.

46. Pfreundschuh M.; Harder, D.; Ucurum, Z.; Fotiadis, D.; Müller, D. J. Detecting Ligand-Binding Events and Free Energy Landscape while Imaging Membrane Receptors at Subnanometer Resolution. *Nano Lett.* **2017**, *17*, 3261-3269.

47 Kimura, Y.; Vassylyev, D. G.; Miyazawa, A.; Kidera, A.; Matsushima, M.; Mitsuoka, K.; Murata, K.; Hirai, T.; Fujiyoshi, Y. Surface of Bacteriorhodopsin Revealed by High-Resolution Electron Crystallography. *J. Mol. Biol.* **1999**, *286*, 861-882.

48 Medalsy, I.; Hensen, U.; Müller, D. J. Imaging and Quantifying Chemical and Physical Properties of Native Proteins at Molecular Resolution by Force-Volume AFM. *Angew. Chem. Int. Ed.* **2011**, *50*, 12103-12108.

49 Pettersen, E.F.; Goddard, T. D.; Huang, C. C.; Couch, G. S.; Greenblatt, D. M.; Meng, E. C.; Ferrin, T. E. UCSF Chimera-A Visualization System for Exploratory Research and Analysis. *J. Comput. Chem.* **2004**, 25, 1605–1612.

50. Ando, T. High-Speed Atomic Force Microscopy Coming of Age. *Nanotechnology* **2012**, *23*, 062001.

51 Sugimoto, Y.; Pou, P.; Abe, M.; Jelinek, P.; Pérez, R.; Morita, S.; Custance, O. Chemical Identification of Individual Surface Atoms by AFM. *Nature* **2007**, *446*, 64-67.

52 Baykara, M. Z.; Todorovic, M.; Monig, H.; Schwendemann, T. C.; Unverdi, O.; Rodrigo, L.; Altman, E. I.; Pérez, R.; Schwarz, U. D. Atom-Specific Forces and Defect Identification on Surface-Oxidized Cu(100) with Combined 3D-AFM and STM Measurements. *Phys. Rev. B* **2013**, *87*, 155414.

53. Oria, L.; Ruiz de Luzuriaga, A.; Alduncin, J. A.; Perez-Murano, F. Polysterene as a Brush Layer for Directed Self-Assembly of Block Co-Polymers. *Microelec. Eng.* **2013**, *110*, 234–240.